

TITAN DR1: An Improved, Validated, and Systematically-Controlled Recalibration of ATLAS Photometry toward Type Ia Supernova Cosmology

ELIJAH G. MARLIN,¹ YUKEI S. MURAKAMI,² DILLON BROUT,¹ JACK W. TWEDDLE,³ BRODIE POPOVIC,⁴ KEN SMITH,⁴ STEPHEN SMARTT,³ DANIEL SCOLNIC,⁴ DAVID JONES,⁴ MARIA VINCENZI,³ JASPER MILSTEIN,¹ AND ERIK PETERSON⁴

¹*Departments of Astronomy and Physics, Boston University, Boston MA 02215*

²*Department of Physics and Astronomy, Johns Hopkins University, Baltimore, MD 21218, USA*

³*Astrophysics sub-Department, Department of Physics, University of Oxford, Keble Road, Oxford, OX1 3RH*

⁴

ABSTRACT

ATLAS (Asteroid Terrestrial Last Alert System) is a transient survey of four telescopes, covering the entire night sky. To date, ATLAS has observed over 10,000 spectroscopically confirmed, type Ia supernovae (SNe Ia), of which thousands are publicly-available cosmology-grade light curves (to be released as TITAN DR1). In preparation for using this massive, low-redshift, all-sky SN Ia dataset in cosmology, we evaluate and cross-calibrate the ATLAS forced photometry in a manner consistent with the SNe Ia literature, utilizing the Dark Energy Survey (DES) year 6 data release, taken on the Dark Energy Camera. The 5000 square degree DES footprint covers sky regions both in and out of the Pan-Starrs (PS1) footprint, allowing us to test the primary calibrating instrument of the ATLAS Refcat2 catalog. An initial evaluation of offsets between ATLAS and DES catalogs are on a ~ 0.01 mag scale, highlighting the impressive robustness and initial calibration of the ATLAS telescope network. We proceed by determining relative delta zero point offsets (in mag) for two different scenarios: 1) pixel to pixel offsets within individual CCDs (reduced to ~ 4 mmag RMS after corrections), 2) chip to chip offsets across each of the 9 CCDs and filters (reduced to ~ 3 mmag RMS after corrections). Finally, we identify the largest source of systematic uncertainty in the analysis coming from an observed transmission function color dependence requiring shifts in the assumed ATLAS filters resulting in biases at the ~ 10 - 20 mmag level if uncorrected. We validate our calibration of ATLAS photometry through (a) CALSPEC standard stars, (b) independent tertiary star catalog, and (c) distance modulus SNe Ia cross-matched to other surveys, and their results show an improved consistency across the ATLAS photometric system. In total we find a preliminary estimate of all calibration-related systematic uncertainties combined in this work to be 5 mmag in orange band and 10mmag in cyan band, facilitating competitive cosmological constraints with the TITAN SN Ia dataset.

Keywords: Cosmology, cosmology: observations, (stars:) supernovae: general

1. INTRODUCTION

Type Ia supernovae (SNe Ia), thermonuclear explosions of white dwarves, are one of the most successful standardizable candles thanks to their known luminosity–color–duration relationship (Phillips 1993; Hamuy et al. 1996; Tripp 1998). The small scatter in the post-standardization luminosity makes SNe Ia an excellent distance indicator for cosmology (e.g., Filippenko 2005). The state-of-the-art measurements of cosmological parameters, including equation of state for dark energy (e.g., DESI Collaboration et al. 2025), use a compilation of SNe Ia samples that cover a wide range of redshifts, such as DESY5, Pantheon+, and UNION3.

A commonality among these datasets is that they combine low-redshift ($z \lesssim 0.1$) and high-redshift ($z \lesssim 1$) surveys. All SNe Ia datasets used in DESI Collaboration et al. (2025), DES (1500 high-z SNe Ia; Abbott et al. 2024a), UNION3 (containing more than 2000 high-z SNe Ia; Rubin et al. 2025) and Pantheon+ (1550 high-z SNe Ia; Brout et al. 2022; Scolnic et al. 2022a) take advantage of overlapping low-z datasets which add up to ~ 200 SNe Ia, (e.g., CfA1; Riess et al. 1999, CfA2; Jha et al. 2006, CfA3-Keplercam; Hicken et al. 2009a, CfA3-4Shooter; Hicken et al. 2009b, CfA4p1, CfA4p2; Hicken et al. 2012, CSP DR3; Krisciunas et al. 2017, LOSS1; Ganeshalingam et al. 2010, LOSS2; Stahl et al. 2019,

SOUSA; Brown 2014, Foundation; Foley et al. 2018, CNiA0.02; Chen et al. 2022). Current constraints of cosmology (Boruah et al. 2020; Riess et al. 2022; Scolnic et al. 2022b; Vincenzi et al. 2024, e.g.) rely on these historical low- z SN Ia datasets to point to interesting new physics (Brout et al. 2022; Abbott et al. 2024b; DESI Collaboration et al. 2025; Tang et al. 2025, e.g.). This reliance on existing low- z datasets will continue to be a challenge for harnessing the full potential of upcoming high- z surveys, such as LSST and Roman, and necessitates the collection and analysis of new datasets collected over many years.

TITAN (Type Ia supernova Trove from ATLAS in the Nearby universe), the low- z SN Ia dataset that we present in a series of papers will provide a solution. TITAN is a compilation of spectroscopically confirmed SNe Ia observed by The Asteroid Terrestrial-impact Last Alert System (ATLAS). ATLAS, a NASA funded all sky survey, visits the whole sky every night with limited magnitudes at $g \sim 20$, making it optimal for capturing low- z SNe Ia up to $z \lesssim 0.1$. The first data release of TITAN dataset, containing $\sim 10,000$ light curves ($\sim 3,000$ cosmology grade with host- z) consists of three papers. The overview, SN Ia light curves, and the Hubble diagram are presented in Murakami et al. (2025) and the simulation and the forward-modeling of observational bias is presented in Tweddle et al. (2025). In this paper, we validate the ATLAS calibration and implement literature standard corrections in preparation for cosmological analysis. In our Gold SNe Ia sample, we find a scatter of $\lesssim 0.17$.

The calibration of datasets, such as Pantheon+, consist of two steps: characterization of surveys' photometric systems (e.g., uniformity of the focal plane, temporal changes in transmission properties, linearity along wavelength and flux levels) and correction for each filter/ detector configuration to a single reference photometric system. Scolnic et al. (2015) (supercal) calculates relative zeropoint offsets using secondary (CALSPEC) stars between PanSTARRS (PS1) and other telescope systems. This method was updated and improved upon in Brout et al. (2022) (fragalistic) for Pantheon+, through the use of tertiary standards in addition to primary and secondary stars. Additionally, they quantify the small variations of transmission functions and its impact on cosmology. Popovic et al. (2025) (Dovekie) is the most recent iteration of this method, providing an open source framework and expanded sets of primary calibration stars with faint DA white dwarves.

For calibration of TITAN, we employ the same techniques to cross-check consistency of the existing ATLAS calibration. ATLAS is a telescope network com-

prised of four telescopes, two in the northern hemisphere ($\text{Dec} \geq -50^\circ$), and two in the southern hemisphere ($\text{Dec} \lesssim +40^\circ$) (Tonry et al. 2018). Of these, the northern telescopes underwent several changes and upgrades of detector setups, resulting in nine total telescope/ CCD combinations, over a decade, since commissioning. ATLAS primarily uses two broadband filters: ATLAS-cyan ($4200 \lesssim \lambda_{\text{obs}} \lesssim 6500\text{\AA}$) and ATLAS-orange ($5600 \lesssim \lambda_{\text{obs}} \lesssim 8200\text{\AA}$) (Tonry et al. 2018). In total, we have 18 possible filter-detector configurations (e.g., chip 0 - cyan = chip 0c), with exceptions of chips 0 and 2 not containing cyan (see Tab. 1 for chip details). In this work we treat each combination as separate filters (similarly to CfA filters in supercal).

The baseline ATLAS calibration, applied to every frame by default, uses Refcat2, an all-sky tertiary star catalog in PS1 system (Tonry et al. 2018). In this work, we use an independent, well-calibrated tertiary star catalog, that covers declination ranges inside and outside PS1 to validate this baseline calibration. We select DESY6 tertiary star catalog (Rykoff et al. 2023). The DES survey is known to have a photometric uniformity of $<1.8\text{mmag}$ and, whose absolute flux is known at the 1% level, making it an excellent candidate for a relative calibration. The footprint of 5000 square degrees also provides a wide range of stellar photometry (with over 17 million observed stars) for us to cross compare with, which is needed, given the all sky nature of ATLAS.

We present the data used in this work, including ATLAS, DES, and synthetic photometry in Sec. 2. In Sec. 3, we quantify and discuss two levels of calibration (intra-chip, inter-chip) needed to prepare TITAN for cosmology. We compare the resulting SNe Ia luminosities with other modern low- z datasets in Sec. 4. We discuss the implications of our findings and their impact on cosmology in Sec. 5, followed by our conclusion in Sec. 6.

2. DATA PREPARATION

2.1. Tertiary Star Samples

For this paper, we build three distinct tertiary star catalogs. First, a baseline sample of randomly distributed stars that are common to both Refcat2 and the DES Y6 catalog (Bechtol et al. 2025). This sample has no preference in color or location: the resulting distribution of these stars are not even across color, and exist in small populations at $g - i$ color ≤ 0.2 , resulting in few stars in the blue. Referred to hereafter as 'color-blind' sample. Second, a subset of the catalog above (common Refcat2 and DES Y6 stars) but only for stars that are blue biased (DES $g - i$ color ≤ 0.2). We use this second sample because our SNe Ia primarily exist

ID	sitecam	Nickname	MJD _{min}	MJD _{max}
0	01a	acam2	57800	58715
1	01a	gold	58719	59465
2	01a	green+fuzzy+4x	59466	59830
3	01a	magenta+wormy+5x	59830	-
4	02a	acam1	57800	58717
5	02a	red	58718	59519
6	02a	red+alien+1	59522	-
7	03a	blue+cruddy+2	59561	-
8	04a	gold+freckles+3x	59605	-

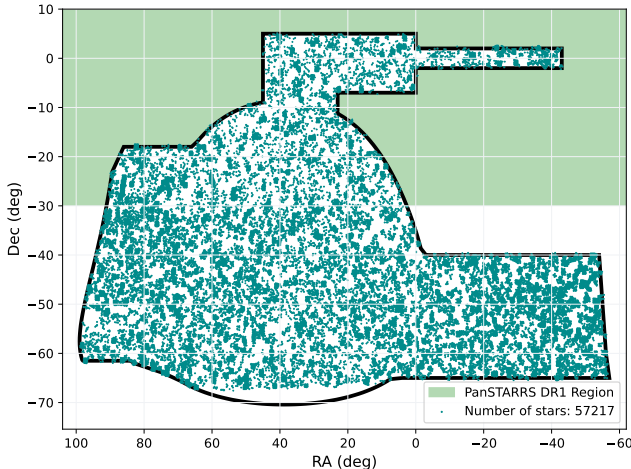
Table 1. Detector configurations

Figure 1. Each individual star field by RA and Dec. Forced photometry from ATLAS is initially in a 0 to 360 degrees RA range and are converted to a 180 to -180 RA range for consistent plotting. The DES footprint is over plotted here as well as the Pan-STARRS region. Note that the southern telescopes take over slightly below the PS1 region at Dec of -50. Stars were chosen in 1 square degree chunks randomly distributed throughout the DES footprint. There are 500 chunks each containing roughly 200 stars in our color-blind sample, and about 50 stars over 500 chunks in our blue sample. In total there are roughly 125,000 stars collected, although this number gets reduced substantially after cuts.

in this color range, and it enables us create a uniform in color, total star catalog, for calibration. Referred to hereafter as 'blue' sample. Third, a baseline sample of randomly distributed stars from DES Y6 that are NOT found in the Refcat2 catalog. These stars functionally similar to SNe Ia, an object whose color and brightness is not used in any part of ATLAS calibration (including initial Refcat2 zeropoint calibration). Referred to hereafter as 'non-refcat' catalog.

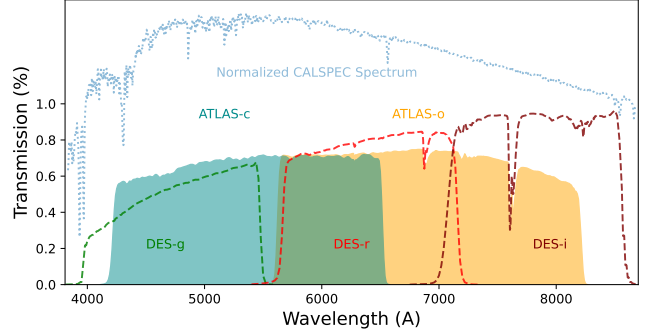


Figure 2. Transmission (as a percentage of light allowed) vs wavelength for ATLAS orange and cyan bands vs the DES g , r , i bands. Data comes from SVO2. Over plotted is one of the CALSPEC synthetic stars used in our calibration. The star's flux density is scaled up arbitrarily, to be visible on the same scale as the filter functions. The y-axis (percentages) values associated with it are relative and not absolute.

For all samples we apply cuts as recommended by the ATLAS team in Tonry et al. (2018). We also apply cuts on stars with excessively large errors (flux $\geq 2000\mu J$), χ^2 above 5, and $17 \leq \text{DES } r \text{ band} \leq 19$ mag.

Fig. 1 shows the locations of the blue + color-blind samples. This figure only includes stars that pass cuts and are used in calibration. Note the even distribution of stars across the DES footprint, with the exception of the absolute lowest section.

Now that we have assembled these three catalogs, we proceed to re-sample our tertiary stars catalogs. We re-sample blue + color-blind catalogs, resulting in a roughly even number of stars above and below DES $g - i$ color of 0. This re-sampled stellar dataset is used in Sec. 3.2. This re-sampling is important because we measure the slope of our observed - synthetic data residual as a function of color for these stars. Having an even distribution of stars across the entire color range is important to avoid bias or not account for slope at a certain color.

Another aspect that is included in the re-sampling is to remove all stars that only contain measurements made by GAIA in Refcat2. We observe a substantial anomaly, particularly at blue colors, in stars observed by GAIA and that have data from no other survey, relative to PS1 stars (which we take as truth). Because of this, and because stars from all other surveys that comprise Refcat2 follow the PS1 trend, we remove these stars from calibration. Additionally, all of these GAIA stars have large error bars. This resolves a potential chromatism at blue colored stars that could bias calibration later on.

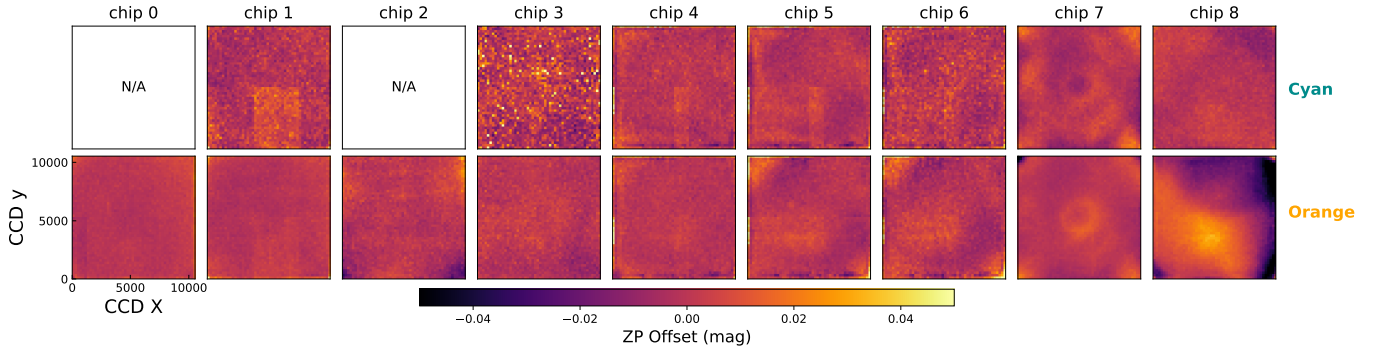


Figure 3. The magnitude residual for all chips by pixel. Median binning applied (50 pixel bins). The heat in these plots have the median residual of each chip subtracted out of them to align the chips residual at 0. The purpose of this part of the calibration is to notice pixel to pixel variations, thus having a constant mag offset does not show much, this allows us to more clearly see discrepancies. Note the right side of chip 8. Chip 8 sees a substantial increase in brightness as x pixel moves right. All other chips look relatively uniform, there are some clear CCD patterns (chip 7, 1) across filters that we can still see post zeropoint calibration.

2.2. ATLAS Forced Photometry

We take our three catalogs and obtain their ATLAS observations by performing the standard forced photometry routine (`tphot`). `tphot` is a custom point-spread-function (PSF) fitting routine: it runs on the difference images of ATLAS forced photometry to produce flux measurements of any source detected 5σ or more above noise level. ATLAS forced photometry is run directly on the ATLAS server side. There is no proper-motion involved in these requests.

2.3. DES Photometry

The DES Y6 survey (Rykoff et al. 2023) is an incredibly robust (<2mmag relative uniformity over the survey region) and well measured survey, covering a large 5000 square degree portion of the sky. Most of the 17 million stars contained within DESY6 have i -band magnitude: $16 < i < 21$. The survey uses a modification of Foward Global Calibration Method (FGCM) from Burke et al. (2017) to remove positional discrepancies across the DE-Cam CCD.

The absolute calibration is done with the Hubble Space Telescope (HST) CALSPEC standard star *C26202* as specified by Rykoff. Including systematic errors, DES calibrates to *C26202* to the 1% level.

2.4. Synthetic Data

We generate synthetic ATLAS and DES photometry with NGSL templates (Koleva & Vazdekis 2012) and CALSPEC standard stars. We take transmission functions for ATLAS from Tonry et al. (2018). We do this by fitting a spectrum of a CALSPEC or NGSL star, to our filter functions wavelength grid. We then integrate this spectrum flux in the photon count space (as opposed to the energy space), and convert this to AB magnitude at

the photon pivot wavelength, where AB mag has to be defined in the frequency space. In order to do this at a large scale, we modified the code from Popovic et al. (2025) to include the ATLAS filter functions. This enables us to produce synthetic stars for all of our filters at different wavelength shifts quickly.

2.5. ATLAS CCD - Filter System

ATLAS's 9 CCDs across two filters, produce 18 total CCD-filter configurations. Chip 0 and 2 never took data in the cyan band, leaving us 16 total CCD-filter configurations. The four telescopes that comprise ATLAS began operating about a decade ago with the first northern telescope starting operation in June 2015 (HKO), the second in February 2017 (LMO), the two southern telescopes began operation in 2021. A critical addition was made to the northern telescopes in 2017, as such we were instructed to only use data after MJD 57800. Fig. 2 shows the flux density of each ATLAS and DES filter as a function of wavelength, with a reference CALSPEC stellar spectrum. We observe that ATLAS's coverage approximately lines up with DES g,r,i bands.

Another key note is that the quantum efficiency (QE) is not uniform across the two northern telescopes. It is essentially uniform until $\lambda = 6500\text{\AA}$, where there is deviation over the rest of the wavelength we use. We do not attribute substantial effects in our calibration with QE. See Fig. 3 in Tonry et al. (2018) for additional details about QE in ATLAS.

3. ANALYSIS

We break our calibration down into two primary components. Firstly, we have the intra-chip calibration, where we have examined CCD chips of each telescope systematically, to determine pixel to pixel trends that we can correct. Secondly, is inter-chip calibration. We

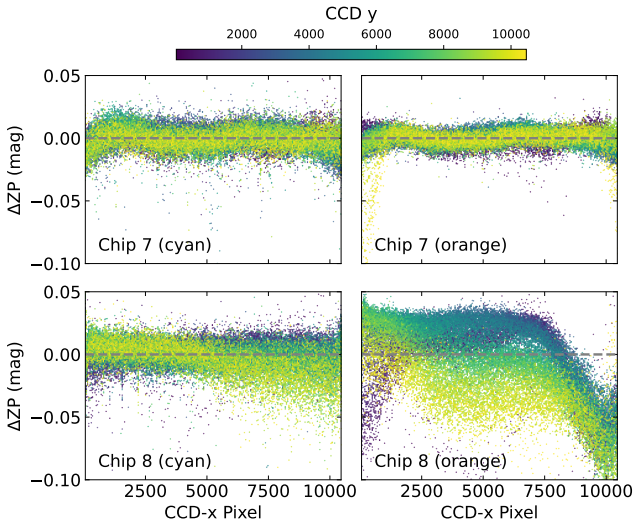


Figure 4. Sliced view of two chips from Fig. 3 in orange and cyan bands. The delta in zeropoint in magnitude is shown on the y axis and the x axis is the x pixel. This shows the significant non uniformity of chip 8o as a function of x pixel. Note how in cyan, although not quite as tight as chip 7 there is no pixel dependent non-uniformity. Chip 7 is a much more typical chip, a tight consistent offset centered at 0 (this oscillation pattern seen here in chip 7, can be seen in the chip 7 heatmap as the circular ring). The sharp dips, especially in chip 7o, on the edges of the chip (50 pixel edge) get cut out when we create the correction function.

looked at trends across all filter-chip combos to produce a median Δ zeropoint offset for each. This portion also includes filter shifts in wavelength, where we shift the filter by some small amount of Å, to correct for chromatic effects in the filters. We conduct this filter shift in a phenomenological manor, focusing primarily on its effects for calibrating for cosmology.

3.1. Intra-Chip Variation

The untargeted, all-sky survey pattern by ATLAS creates a dither pattern around each star’s coordinate. This pattern provides an insight into the sensitivity function’s possible variations within each CCD, as the same object is measured at different CCD coordinates.

ATLAS CCDs have 10000X10000 pixels, and each image is read out in 1x1-binning by default. With the typical median seeing of 0.5” (Lyman et al. 2020), this spans approximately one pixel. The `tphot` forced photometry routine reports the CCD coordinates (x,y) that correspond to the requested sky coordinates for the forced photometry. We use this information to construct the coordinate-dependent zeropoint offset map within each chip.

The procedure is the following: for any given star, we have multiple observations across different x,y coordinates in each CCD. Then for any star with data in a given CCD, we take the weighted mean of all magnitude values, and subtract that from each individual pixel to pixel magnitude value. This creates a coordinate dependent offset of one star mapped across all chips. We then repeat for every star and layer the results. Fig. 3 shows the results of this process.

When looking at Fig. 3 chips 0-7 have little to no noticeable pattern, i.e. pixel to pixel variation. We can see some repeat patterns, even post zeropoint calibration, in chips 1, 4, 7 for example, in both filters. Since these are different filters and thus, completely independent datasets, this is a strong validation that these patterns (and those more significant like chip 8o) are physical, and not a product of our data processing. We are ignoring edge effects on all the chips as those are notoriously unreliable across CCDs, thus they are cut out, at the 50 pixel scale, before correcting.

Chip 8 has a significant vignetting pattern toward the right side. In chip 8 we can see brighter magnitude residuals toward the right side and slightly at the top of the chip. Fig. 4 shows a scatter plot of the x and y axis of chip 1 on the top plots, and the same plot except for chip 8 on the bottom. Clearly visible here is the trend in the x axis of the chip toward brighter observations on the right. A significant observation from Fig. 4 is that this vignetting pattern, producing brighter observations in chip 8o, only exists in the orange band.

We account for this vignetting pattern in our correction model, allowing us to use chip 8o despite its large aberration. We create our correction model by binning the pixels of each chip into 50 pix bins. We use our calculated ‘optimal smoothing radius’ of 540 pixels, to convolve our 2D arrays using python’s `Gaussian2DKernel`. This convolution then gets remapped to the entire 10,000 by 10,000 pixel space to produce a complete correction map for one chip. Our model applies unique corrections to each chip and each filter separately (16 total correction maps). These maps are then merged together and applied to our calibration. This comprises the intra-chip correction.

3.2. Inter-Chip Variation

The inter-chip offset is described as the vertical shift between the observed ATLAS - DES transformation and the synthetic transformation in Fig. 5. The residual plot on the bottom of this figure shows the value of this vertical shift. The residual is calculated as the y axis difference between the real data at that color and the synthetic polynomial. The synthetic polynomial is a 5th order approximation of the synthetic data using python’s `Polynomial.fit`.

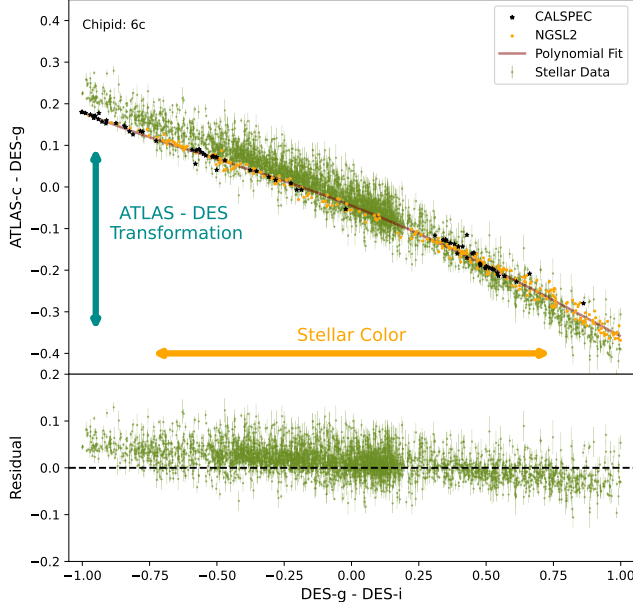


Figure 5. ATLAS - DES transformation (ATLAS-c - DES-g) on the y axis with DES color on x axis. Real stellar data (green), over plotted with NGSL and CALSPEC synthetic stellar photometry. A 5th order polynomial is fit to the synthetic data (brown) to show its shape. Bottom plot is the synthetic - real residual plotted on the y axis. This specific plot is for chip 6c. The vertical shift used to calculate the offset of each chip-filter combo, is the real data - the synthetic trendline at that x coordinate shown in this plot. The actual calculation is substantially more complex than what is shown here, please see Appendix A for details. The lower residual plot, shows the chromatic slope that must be accounted for. Note: this is the most obvious example of our need for correction, see Fig. 7 for the result of the residuals across all chips.

We expect that this residual is a flat line centered away from 0. The amount this line is offset from 0 would be the zeropoint offset of this chip-filter combination (there is a collapsed likelihood function used here, but it is still the result of this residual). This is the zeropoint offset because, the synthetic data uses CALSPEC stars, which have the absolute, true flux, of our filter function. The amount offset the observed data is, is thus the offset of our physical filter from truth.

Notably, there is a $g - i$ -color dependent trend in the residuals. Considering that this is a residuals of observed photometry from the synthetic photometry, the presence of slope implies that our the filter transmission function used for the synthetic photometry differ from each telescope-detector-filter combinations' actual throughput. This is not an unusual observation: previous cosmology-grade calibrations of SNe Ia catalogs, such as Brout et al. (2022) and Popovic et al. (2025) have identified the slopes using similar method. Unless

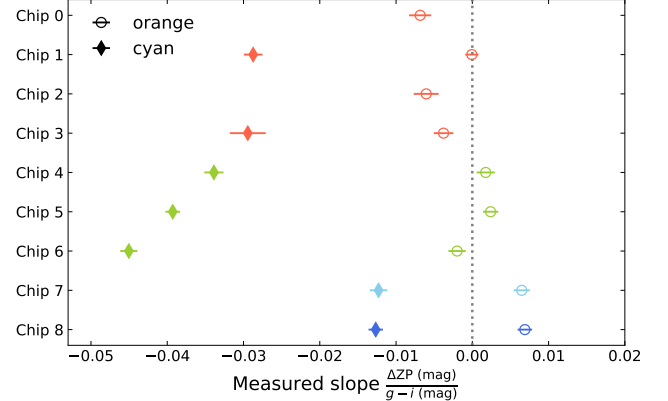


Figure 6. Whisker plot, with chip on the y axis and the measured slope of the residual (shown at the bottom of Fig. 5) on x axis. On x axis, ΔZP represents the mean offset between real ATLAS - DES data and synthetic which can be seen visually in Fig. 5. Colored by which telescope each chip corresponds to. Orange band is tightly packed around no slope, with an average close to 0. Cyan band is consistently negative sloped, indicating a chromatic offset. Chips 4,5,6 (all same telescope over time) get progressively worse, this could indicate a physical problem with the filter that worsens each time the CCD is switched. Chip 7,8 represent the newer 2021 telescopes, and have a much smaller slope, potentially the result of a correction to the cause. The larger the slope value the larger the wave shift we apply, thus, this plot, indicates the significance of the shift.

a careful, laboratory-level re-measurement of the system throughput can be immediately performed, these slopes are typically corrected by applying modifications to each filter's transmission function. Fig. 7 demonstrates the color-dependent (chromatic) effect of such modifications: two distinct methods (wavelength-shift and filter-filt; see Popovic et al. 2025 for review) produce a nearly identical color-dependent changes in the predicted magnitudes. For consistency with the literature and simplicity, we choose to employ the wavelength-shift method. A correct choice of wavelength shift can match the measured slope in the tertiary stars, essentially mitigating the chromatic effect during the light-curev fitting of the cosmological SNe Ia samples.

The results of applying this shift means, that, in cyan we shift each chip by approximately 50 - 100 Å in the same direction. Although this initially sounds substantial, given how broad the ATLAS filter bands are this would essentially be the equivalent of shifting a DES band 25 - 50 Å. Still, shifting a filter function this much is not physical, it can result in shifting through telluric lines for example. While we understand this is not the physical cause of the chromatic slope, we take a phenomenological approach because, this approximation fits

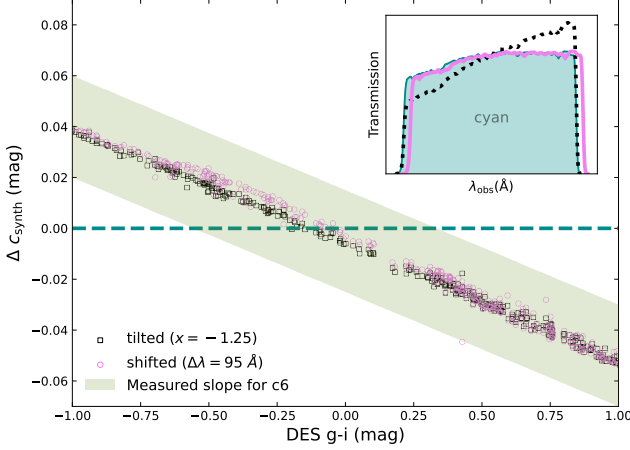


Figure 7. This shows results for chip 6c, the same chip in Fig. 5. The Y axis is the synthetic magnitude of cyan band with no shift minus the magnitude with a shift, showing how we shift our synthetic values at each color. X axis is DES g-i color. A green line is over plotted to show the observed slope in the residuals. The subplot in the top right corner shows the original, shifted, and tilted transmission functions. The tilt is -1.25 and the shift here is 95 Å. Note, this is a particularly intense slope, see Fig. 7 for the all slope values.

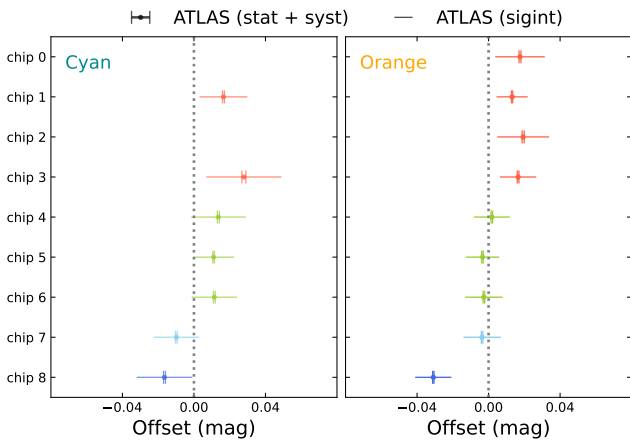


Figure 8. Chip on y axis and offset in magnitude on x axis, in the orange and cyan bands in ATLAS. This offset is the vertical shift of the real data from the synthetic data in ATLAS-DES transformation vs color, as demonstrated in Fig. 5. This is condensed down to a single value across multiple colors and DES filters. See Sec. A for details. Two error bars are displayed here, one (small) representing the statistical error in the physical ATLAS data, and the other (large) representing corresponding to the dispersion of the data (intrinsic scatter).

extremely well, and is backed up in the literature as a viable solution for cosmology.

Table 2. Orange and cyan band zero-point offset corrections and wavelength shifts for TITAN calibration. zeropoint offset corrections are in units of magnitude while wavelength shift is in units of Å.

Chip	Δm_c (mag)	$\Delta \lambda_c$ (Å)	Δm_o (mag)	$\Delta \lambda_o$ (Å)
0	-	-	+0.176	+22
1	+0.017	+56	+0.013	+5
2	-	-	+0.019	+25
3	+0.028	+57	+0.017	+27
4	+0.014	+67	+0.002	-6
5	+0.011	+78	-0.003	-6
6	+0.011	+87	-0.003	+10
7	-0.010	+28	-0.004	-15
8	-0.017	+28	-0.031	-21

3.3. Reference Catalog Validation

For each forced photometry image we collect from ATLAS there is a zero-point calculated using stars from the Refcat2 catalog. This catalog is a combination of many different surveys to get an all sky coverage that corresponds to ATLAS. The primary surveys involved here are PS1 and GAIA (Tonry et al. 2018).

We validated that no single survey was providing chromatic or skewed data results, thus biasing our photometry. The refcat2 catalog combines every survey that measures a star and averages their results together, as such, there is no clean way to determine the component only one survey contributes to that result. Thus, we look mostly at stars that only have contribution from one survey, or are specifically missing contribution from one survey. Our primary finding was that, in the blue region, stars that are only measured by GAIA are skewed substantially off the main PS1 branch. This could result in a bias from the GAIA data. To avoid this potential data skewing, we filter out the stars that only appear in GAIA.

Other than the discrepancy with GAIA, the rest of the surveys match well with the trend of PS1, including the other surveys that make up the catalog that do not contain any data from PS1. For this reason we say that we trust the rest of our surveys.

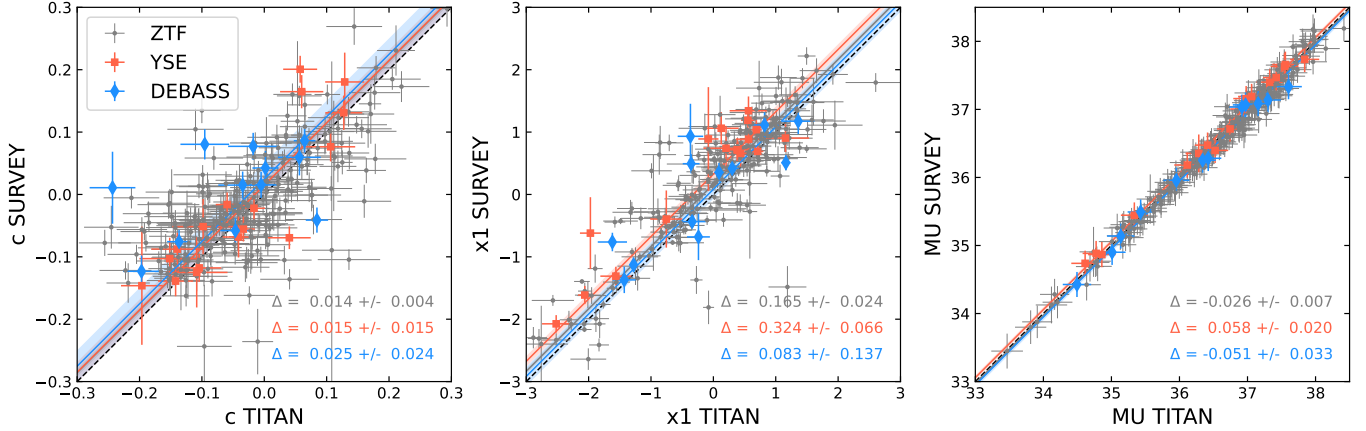


Figure 9. Comparison of TITAN SNe Ia with other modern low- z surveys. TITAN light curves are presented in the companion paper Murakami et al. (2025). Compared against, ZTF DR2, DEBASS 0.5, YSE DR1. Plotted is Color, stretch (x_1), and distance modulus (MU). We use a conservative color error cut of $c_{\text{Err}} < 0.1$, because there only being two bands in ATLAS means we can easily have a SNe Ia light curve without sufficient data in both bands. Due to the sizes of the datasets we are comparing against our matching with ZTF has over one thousand matches, while DEBASS and YSE have tens and hundreds of matches respectively. This is likely a major contributor to the significant errors on those comparisons in MU.

4. DISTANCES AND HUBBLE DIAGRAM RESIDUALS

We fit SNe Ia parameters x_1 (stretch), color, and μ (distance modulus) in SALT3. All share the same coefficients in gamma, alpha, and beta. Fig. 9 shows a comparison between TITAN and three other low- z surveys. We spatially match our SNe against those of other surveys to get relative distance trends. We specifically compare against ZTF, DEBASS, and YSE. Notably, Foundation is absent from this comparison. This is because we didn't have enough spatial matches of SNe Ia to say anything significant.

We demonstrate that our distance indicators (a significant benchmark) from our TITAN SNe, after calibration are in line with other state of the art low- z supernova experiments.

4.1. ZTF

ZTF (Zwicky Transient Facility) SNe Ia data release has released 2667 spectroscopically confirmed type Ia SNe with matching redshifts in the low- z region ($z < 0.3$) that pass initial cosmology cuts Rigault et al. (2025). This is one of the largest spectroscopically confirmed low- z supernova datasets to date. Note that ZTF has not completed their cosmology grade calibration, and acknowledge an offset in their dataset. We compare to ZTF as the only other low- z sample with SNe on the same order of magnitude as TITAN.

4.2. DEBASS

DEBASS (Dark Energy Bedrock All Sky Supernova program) has delivered the largest uniformly calibrated low- z dataset of the southern sky to date Sherman et al.

(2025). They have already released 77 spectroscopically confirmed SNe that pass cosmology cuts Acevedo et al. (2025). DEBASS operates in the southern sky with a similar redshift range as TITAN ($0.01 < z < 0.08$). Given that DEBASS operates off of DECam, which ATLAS is now calibrated to, this should enable excellent cross matching of SNe Ia once DEBASS DR1 is released and we can find hundreds of matches.

4.3. YSE

YSE (Young Supernova Experiment) comprised of data from ZTF and PS1 contains 451 spectroscopically confirmed and cosmology grade SNe light curves. Their redshift range reaches a bit higher than TITAN ($z < 0.5$), yet this is still a strong comparison for our low- z dataset Aleo et al. (2023).

4.4. Comparison of SALT3 Parameters

Fig. 9 gives us a high degree of confidence in our calibration of SNe Ia, and ATLAS's ability to produce reliable light curves. Note that there is a cut on color error at $\sigma_c < 0.1$ (see discussion in Murakami et al. 2025). The left most plot shows this through the minimal scatter of TITAN SNe Ia relative to other surveys. There is not a consistent positive or negative offset between TITAN and the other surveys indicating a lack of systematic difference.

There is an average offset of ~ 0.17 , 0.32 , 0.08 for the stretch parameter x_1 . Though both ZTF and YSE offsets are significant, the offset values significantly differ from each other, and the exact degree of systematic discrepancies is difficult to measure from this dataset alone. We will discuss this effect in Murakami et al.

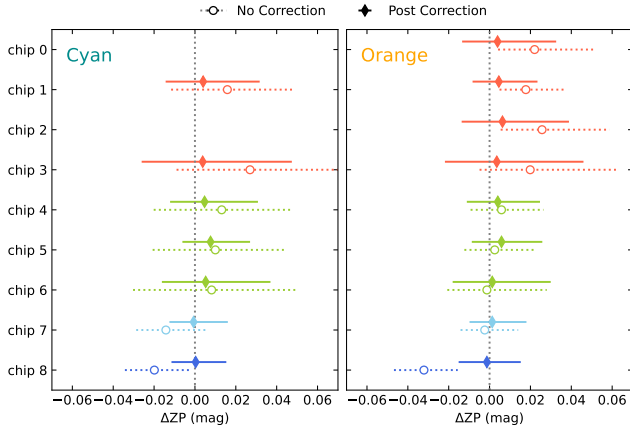


Figure 10. ΔZP offset in magnitude between real and synthetic ATLAS - DES transformed tertiary stars on x axis. The ΔZP value is the offset between chips and is corrected by the inter-chip correction. The error on the values is the result of a projection of the residuals from Fig. 5 into the ΔZP offset space, representing the scatter in residual. This error is dominated by the chromatic slope displayed in Fig. 6. Note, the data used for these calculations is completely independent from the stars used in calibration ('non-Refcat2' data), and are not in Refcat2. Can see that in both Orange and Cyan the ΔZP offset improves significantly after inter-chip correction. The error also improves in both cases, although substantially more in cyan as the slope gets significant corrections compared to orange. This plot shows a validation of inter-chip and chromatic slope calibration. Note, intra-chip correction is already applied to both pre and post correction data.

(2025). Color is relatively consistent with some notable outliers. We believe the fact that there are only two filters in ATLAS produces these outliers, occasionally one of the filters will have too few measurements close to SNe Ia peak.

5. DISCUSSION

5.1. Validation with Independent Tertiary Catalog

We validate our calibration using stars that are not contained in the Refcat2 catalog. These stars are in the DES catalog, however, we run forced photometry on them. This provides a completely independent dataset for our validation. These stars are not in Refcat2, thus are not used for the initial frame-by-frame zeropoint calibration, and because our calibration stars are produced by querying Refcat2, these stars are independent from the calibration presented here. This means that from the perspective of ATLAS, these stars behave functionally the same as SNe Ia, a stellar object which the calibration has no prior knowledge of. Fig. 10 displays the effect our calibration has on these validation stars. Additionally, the error bars on these points represent the percentile

range (16th percentile to 84th percentile) of the median values of the net offset of a chip.

If our calibration were to be successful, we would expect to have a higher intrinsic scatter before corrections are applied, due to the slope of the residuals when projected in the the offset space. This should be especially true in cyan band (see Fig. 6). Additionally, we would expect to see our zero point magnitude close in on zero after corrections, due to the inter-chip correction.

Fig. 10, shows both of these to be true. Scatter, especially in cyan band (error bars), is reduced, and all of our offsets are closer to zero. Note chips 4c, 5c, 6c, all of whose scatter is reduced substantially with correction, these chips had some of the greatest initial chromatic slopes. Also note chip 8o, for example, whose delta zero point offset shifts substantially with the inter-chip correction. We find an initial offset of: 0.0169 in orange, and 0.0155 in cyan which get corrected to 0.0023 and 0.0027 respectively. Yielding an 86% reduction in orange band, and 83% reduction in cyan band offsets. We also find that the scatter is reduced by 1% in orange and 28% in cyan. This follows from our expected results, orange has minimal chromatic shift, while cyan's is large. This demonstrates that we are able to correct for that with our filter wavelength shifts.

5.2. Validation with CALSPEC & DAWD Reference Stars

We use a combined dataset of spectroscopic standards, CALSPEC (Bohlin et al. 2014) and DA-type faint White Dwarfs (hereafter DAWD; Boyd et al. 2025), to further validate our results and quantify systematic uncertainties. These spectroscopic standards, observed by *HST/STIS* with an absolute calibration to the physical units, provide a direct comparison of synthetic and observed spectra without the need of deriving the synthetic color-color transformation (Eq. A1). This independency, along with the broadly accepted use of the CALSPEC stars for photometric calibration, makes them an excellent probe to test the possible systematics in the post-correction photometry in TITAN dataset.

In addition to enabling an independent check of our tertiary star-based methods, the use of CALSPEC stars is relevant to the original calibrations of DES and ATLAS. DES uses a single primary calibrating star's spectra for its calibration to the absolute AB magnitude system, HST CALSPEC C26202. DES claims that, including systematic errors, the absolute flux is known at approximately the 1% level. DES generates these synthetic magnitude by integrating the official DES passband throughputs with one of standard spectra for C26202 from the Hubble Space Telescope (HST) Cal-

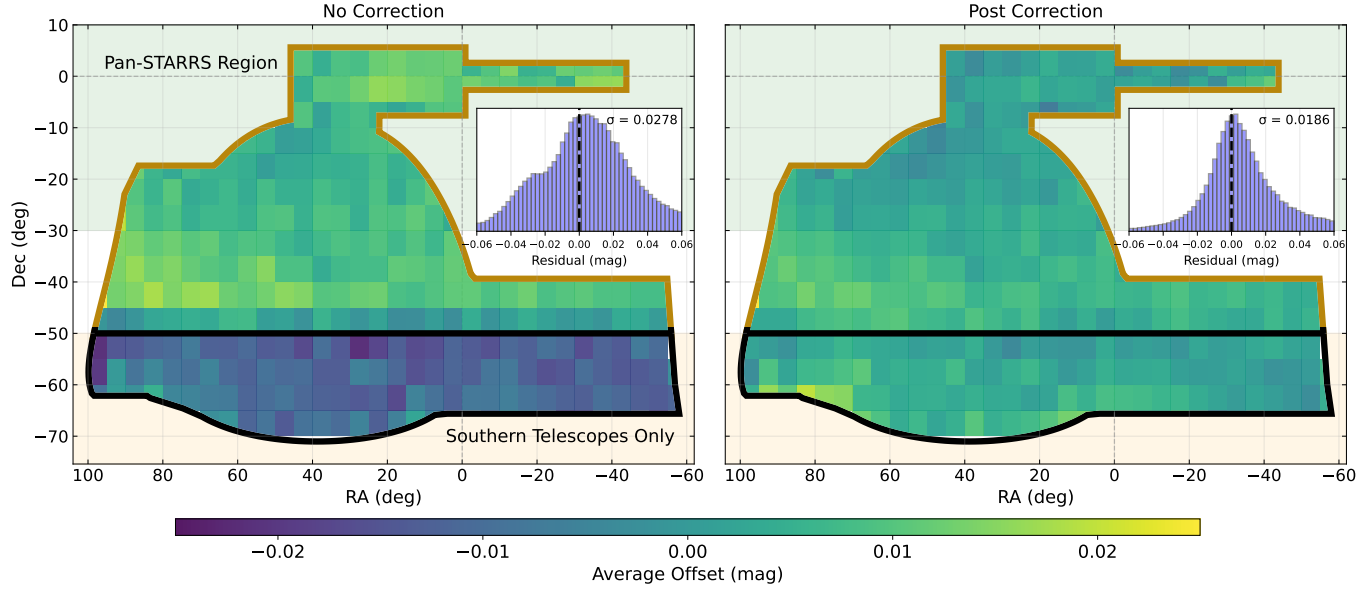


Figure 11. Heatmap of median offset as a function of spatial position. Correction applied here is inter-chip and chromatic shift. Clearly see that we improve the spatial dependence, and that the standard deviation improves. This is most noticeable around -50° declination where the northern telescopes cut off. Can see that the histogram becomes substantially more gaussian after correction.

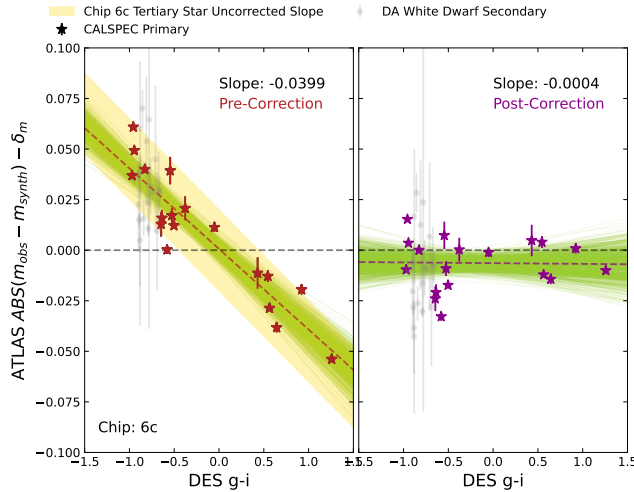


Figure 12. Absolute value of synthetic minus observed residuals of several CALSPEC stars, including C26202, and DAWD, on the y-axis in ATLAS cyan band. Here δ_m is subtracted out. X axis is DES color in $g - i$. The many green lines represent random slope draws to account for covariance, shows a range of possible fitted slopes. The dotted lines are the median slope and the value displayed in Fig. 13. Post correction includes wave-shift and inter-chip offsets. The tertiary calibrator slope from Fig. 6 in chip 6c is overplotted pre-correction in gold. A small offset δ_m is subtracted to account for the small numerical differences and make the shown values compatible with the absolute calibration of DES.

Spec database (Bohlin et al. 2014). PS1, on the other hand, does not use a single CALSPEC star for its ab-

solute calibration: instead, they rely on Ubcral from Schlafly et al. (2012) for the initial zeropoint calibration, which is then tied to the physical units using multiple CALSPEC standards (Magnier et al. 2020).

In Fig. 12, we present the measured offset between synthetic and ATLAS-observed photometry of the chip c6. An additional mmag-level offset $\delta_m = m_{C26202}^{DES} - m_{C26202}^{synth}$ is subtracted to account for the difference between DES photometry of their absolute-scale calibrator, C26202, and our synthetic photometry. This is possibly due to the small, numerical effect from the difference in sub-sampling along the wavelength axis. We optimize a slope and offset $\Delta ZP_i = \mathcal{A} \cdot (g - i)_i + \mathcal{B}$ (the purple line in Fig. 12) in our post-correction residual. We use the values of the slope (\mathcal{A}) and the intercept (\mathcal{B}) to quantify systematic uncertainties.

We see in Fig. 12 that, our corrections improves the chromatic effect. Our slope is reduced from -0.0399 to -0.0004 . This is a validation of methodology of our tertiary star calibration, showing we see nearly the exact same effective slope in primary and tertiary calibrators and are able to correct it. We do not present any orange data for primary calibrators in this plot, orange band data already has minimal slope and our correction is extremely small. We show chip 6c an an excellent validation of our filter-shift correction. We will discuss the resulting reduction of systematic uncertainty in Sec. 5.5.

5.3. Chromatic Effects

Our calibration corrects the chromatic effect, which we observe as a $0.005 - 0.045$ mag-level difference in zeropoint across the $g - i$ range corresponding to the TITAN SNe Ia color. This effect is most notably seen in cyan band on the sitcam 02a telescope, as shown in Fig. 6.

Note that the slope is much stronger (and not centered at zero) in cyan band, this suggests there is a filter problem, not CCD. Also note that chips 4c, 5c, and 6c, which are all on the same telescope, have the largest slopes, and get progressively larger with time. Chips 7c, 8c, are the newest telescopes and have the smallest cyan slope.

These patterns suggest to us several possible physical causes of this chromatic slope. First, quantum efficiency (QE) measurements between the telescope could be off in a systematic way. Second, the definition of the filter function in cyan could be different slightly than the physical filter. The trend in chips 4c, 5c, 6c suggests the possibility that something is repeatedly adjusted in the telescope that shifts the filter in some way.

5.4. Coordinate Dependence

When calibrating four independent telescopes it is important to verify there is no coordinate dependence. There are two main spots we might expect coordinate dependence: at -50deg declination where the northern telescopes cut off, and -30deg declination where PS1 (the primary calibrating instrument of ATLAS) cuts off.

In Fig. 11 we can see, before calibration, there is a coordinate dependent offset at the northern telescope cutoff. We are able to remove this offset with our interchip corrections as seen in the right side of the plot.

- We see that before correction there is a split at -50 dec not so much at -30. Explain why at -50 and not at -30 (good refcat). - Discuss what we don't see. We don't notice any particular patch that is unique. There is no RA dependence as expected. Discuss what changes after applying correction. Scatter reduces, and the clear offset disappears. If it happens: we try fitting gaussian, we get a better fit to a gaussian with correction.

5.5. Systematic Uncertainty

In this paper we present some initial systematic uncertainties for cosmology. The first is the systematic uncertainty on the intra-chip correction. This is calculated as the standard deviation of the offset across all pixels (sec. 3.1). To determine this systematic post calibration we subtract out our correction map from the real observed in Fig. 3 recalculate the standard deviation of the offset per pixel. In Tab. 3, we see a 3mmag improve-

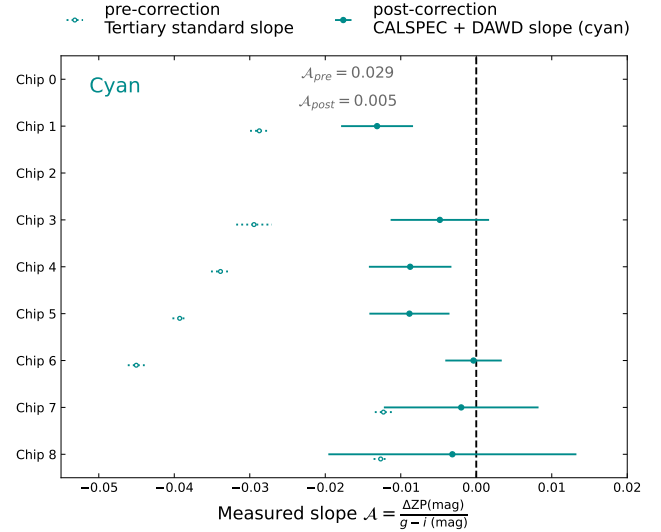


Figure 13. Systematic uncertainty in the cyan band due to the chromatic effect. X axis is the right side of Fig. 12, averaged across all of the random draw slope values. The pre-correction slopes come from the tertiary star slope found in Fig. 6. We find particularly large uncertainties for chips 7, 8 (~ 0.010 and ~ 0.016 respectively). Our systematic uncertainty is calculated as the median of the slopes, across all chips pre, and post correction.

ment across both bands, which is substantial given that the initial effect is only 7mmag.

Second, the magnitude error floor, is the systematics on our inter-chip correction (sec. 3.2). The calculation is the following: we take the values presented in Fig. 10 and take the standard deviation of those points for each filter. We repeat this on data before and after the calibration to verify that our calibration improves the error floor. Tab. 3 shows that our systematic uncertainty in error floor improves in both orange and cyan (by 88% and 81% respectively).

Next, we quantify the systematic uncertainty related to the chromatic effect and our correction (Sec. 3.2, 5.3) using our CALSPEC validation set. We define this systematic uncertainty as the possible range that the TITAN SNe Ia dataset may experience due to their observed color. This is practically propagated from the observed slope in the CALSPEC residuals using the SNe Ia color distribution ($-0.97 \leq g - i \leq -0.11$ mag at 2σ tails, covering 95% of the dataset) measured in Murakami et al. (2025).

Finally, we quantify our confidence in the absolute calibration of ATLAS using HST CALSPEC stars. We take the fitted offset (intercept of the slope at $g - i$ color = 0) after the wave shift has been calculated. The systematic before calibration then = Median(ABS(Offset)) - δ_m . After calibration = =

Table 3. Average systematic uncertainty values per filter before and after calibration. Values are in magnitude.

Systematic	orange		cyan		Description ^a
	Before	After	Before	After	
Intra-chip (pixel-to-pixel) variation	0.007	0.003	0.008	0.005	$\sigma(\Delta ZP_{\text{pixel}})$ in Fig. 3
Inter-chip (chip-to-chip) variation	0.017	0.002	0.016	0.003	$\sigma(\langle \Delta ZP \rangle_{\text{chip}})$ in Fig. 10
Chromatic Effect	0.004	0.003	0.029	0.005	Median slope (\mathcal{A}) \times SNe Ia color range (Sec. 5.5, Fig. 13)
Absolute Calibration	0.012	0.003	0.007	0.006	Median size of CALSPEC offsets, think Fig. 10 from Fig. 12
Total	0.022	0.005	0.035	0.010	

^aFigures are cited here for reference purpose only, as they may only show measurements made before or after correction. We measure the same quantity before and after applying our correction models to quantify the reported values in this table.

Median(ABS(Offset)) – (interchip) – δ_m . This is essentially, an independent validation of only our inter-chip correction using primary calibrators. We specifically use data post-wave-shift for both the pre, and post calibration systematic, as the wave-shift systematic is already contained within row 3 of Table 3 (sec. 5.5, Fig. 13). We find a 9mmag, and 1mmag improvement for orange and cyan bands respectively.

Before our correction, the median slopes for each filter is $\frac{\Delta ZP}{g-i} \sim 0.029, 0.004$ for cyan⁵ and orange band, respectively (see Fig. 6). This corresponds to ~ 0.026 and ~ 0.003 mag-level changes in the zeropoint across the color range of SNe Ia. This slope is consistent across our tertiary catalog and the primary, CALSPEC validation set. After applying our corrections derived from the tertiary star catalog, the remaining slope in the CALSPEC stars become considerably small (0.005), making the systematic uncertainty consistent across filters at $0.005 \frac{\text{mag}}{g-i \text{ mag}} \times (-0.11 - (-0.97)) \text{ mag} \approx 0.0043$.

Table 3 demonstrates that before our correction, we have a total systematic of 22mmag, 35mmag in orange and cyan bands respectively. After calibration we are able to reduce these numbers to 5mmag, 10mmag respectively, presenting a 77% and 71% reduction in systematics respectively. This is lowest relevant sensitivity for TITAN cosmology. For reasons discussed in Murakami et al. (2025), we find that in SNANA we must add a 10mmag error floor to our TITAN SNe Ia already. This implies that our additional systematics from calibration are on a scale to not significantly impact our SNe Ia dataset.

⁵The slope for cyan band varies by a factor of a few between detectors. We use the median values for each filter as a representative value solely for the comparison with the post-correction size.

6. CONCLUSION

SNe Ia are a well proven tool for measuring relative distances for use in cosmology. Until now, most major SNe Ia cosmology surveys have relied on the same 200 low-z SNe Ia. TITAN aims to fix this by providing the largest, independent, spectroscopically confirmed low-z SNe Ia dataset to date. TITAN, which uses the ATLAS all sky survey, must be calibrated using literature proven standards before it can be used in cosmology. That calibration has been presented in this paper.

We conduct a relative calibration between ATLAS and DES, a well measured survey that contains data inside and outside of PS1 (the primary calibrating instrument of ATLAS). In order to do this calibration we queried three distinct tertiary calibration star catalogs. The first (raw), containing a color uniform random sample from across the DES footprint, was produced matching Refcat2 stars with DES and then running forced photometry on ATLAS. The second (blue), containing a color sample that is biased blue to match the color range of SNe Ia and account for the redder nature of Milky Way stars, is produced in the same method as the first. The final catalog (non-Refcat2), is a subset of stars that do not exist within Refcat2 (reverse matched), but are matched with DES before querying ATLAS. This catalog provides a completely independent dataset that mimics the behavior of SNe Ia in ATLAS. We also generate synthetic data using CALSPEC and NGSL standard stars, produced via a modification of Dovekie.

We examine pixel to pixel variations in each CCD and filter (intra-chip). We find most are consistent to the 0.01 level, with the exception of chip 8o, where we notice a significant vignetting pattern. To account for the variations in pixel we build a correction map. This is produced by binning the data, smoothing at the optimal pixel radius, then remapping to the 10,000 x 10,000 pixel CCD. We separately produce a map for each chip filter combination.

Looking at a larger scale we create a correction between each CCD and filter (inter-chip). To do this we calculate the vertical shift in DES - ATLAS transformation and stellar color between the observed data and our synthetically produced data. The offset produced here constitutes our inter-chip correction. Notably, the synthetic - real residual is not flat at a constant value above or below 0, there is a slope. This means that there is a color dependence on our transformation, especially in the cyan band. We find that we can correct for this by applying a shift in the wavelengths of the filters, as has been done previously in the literature. This shift corrects for the slope and reduces the need to inflate the systematic uncertainty to account for it.

We validate this calibration by reviewing a spatial map of the residuals. We find that after our inter-chip correction and filter shift that we notice no position dependent variation. We also see that after our correction our $\Delta_{\text{zeropoint}}$ offsets and their respective errors are reduced. This validates that our correction is in fact improving our stellar photometry.

In addition to our relative calibration using tertiary stars, we discuss an absolute calibration of ATLAS and

its Refcat2 catalog. We compare DES, with an absolute calibration to 1%, to ATLAS using primary calibrators, CALSPEC stars. We look at the magnitude difference between synthetic and observed values for these specific stars. We find that while Refcat2 is not initially well calibrated on an absolute scale our calibration to DES brings it much closer, especially in cyan band.

The calibration above serves as a baseline for the upcoming cosmological analysis, that will result from what we are releasing as TITAN DR1. The light curves and simulations will be presented in [Murakami et al. \(2025\)](#) and [Tweddle et al. \(2025\)](#) respectively.

ACKNOWLEDGEMENTS

We would like to thank the ATLAS team for assistance in gathering massive amounts of forced photometry and for their conversations about the difference imaging pipeline and nuances of the telescopes.

We thank the Hariri Institute at Boston University, for their generous funding contributions to this project.

APPENDIX

A. MULTI-COLOR JOINT LIKELIHOOD ANALYSIS

In Sec. 3.2, we fit a single offset value to an ATLAS filter so that the empirical ATLAS-DES filter transformation matches synthetic prediction. This transformation is color-dependent, and there are multiple possible combinations of DES filters (e.g., ATLAS-o \rightarrow DES-g as a function of color DES-g-DES-i). Each of the combination can be simultaneously evaluated to form a joint likelihood, and we describe the formalism of our likelihood function and the process to prepare necessary quantities below.

First, assuming that the DES filters and their star catalog values are well-calibrated, we obtain an ATLAS offset for each (i-th) star as the following:

$$\Delta_{i, x1, x2, y1, y2} = m_{i,y1}^{\text{ATLAS}} - m_{i,y2}^{\text{DES}} - f_{y1 \rightarrow y2}^{\text{synth}}(m_{i,x1}^{\text{DES}} - m_{i,x2}^{\text{DES}}), \quad (\text{A1})$$

where m represent observed magnitudes of stars, with subscripts $y1$ for the ATLAS band of interest and $x1, x2, y2$ for DES bands we use as a reference. Considering the overlaps of the sensitivity functions, we use the combinations of filters shown in Table 4. We note that there are two exceptions in the listed combinations: the dataset obtained with $(y1, y2, x1, x2) = (c, g, g, r)$ is linearly identical to (c, r, g, r) , and it causes the covariance matrix we describe later to be nearly singular. To avoid this issue and considering that it adds nearly no information, we exclude such combination. Similarly, another combination for the orange filter (o, i, r, i) is excluded. The synthetic transformation function between ATLAS filter $y1$ and DES filter $y2$ $f_{y1 \rightarrow y2}^{\text{synth}}$ is obtained by fitting a third-order polynomial to a fully synthetic data m' ,

$$y^{\text{fit}} = f_{\text{synth}} = \text{Poly}_3(x), \quad x = m'_{x1} - m'_{x2}, \quad y = m'_{y1} - m'_{y2}. \quad (\text{A2})$$

After evaluating Δ_i for each of the combination, we obtain a vector of offsets $\mathbf{r}_i = (\Delta_{i1}, \Delta_{i2}, \dots, \Delta_{i5})^\top$. Due to repeated uses of data, these measurements are not independent from each other, and we quantify that effect by constructing a filter-to-filter covariance matrix for each star. Propagating uncertainties from each observed quantity

Table 4. Combinations of filters used for the offset analysis.

#	ATLAS- <i>c</i>				ATLAS- <i>o</i>			
	<i>y</i> 1	<i>y</i> 2	<i>x</i> 1	<i>x</i> 2	<i>y</i> 1	<i>y</i> 2	<i>x</i> 1	<i>x</i> 2
1	ATLAS- <i>c</i>	DES- <i>g</i>	DES- <i>g</i>	DES- <i>r</i>	ATLAS- <i>o</i>	DES- <i>r</i>	DES- <i>g</i>	DES- <i>r</i>
2	ATLAS- <i>c</i>	DES- <i>g</i>	DES- <i>r</i>	DES- <i>i</i>	ATLAS- <i>o</i>	DES- <i>r</i>	DES- <i>r</i>	DES- <i>i</i>
3	ATLAS- <i>c</i>	DES- <i>g</i>	DES- <i>g</i>	DES- <i>i</i>	ATLAS- <i>o</i>	DES- <i>r</i>	DES- <i>g</i>	DES- <i>i</i>
4	ATLAS- <i>c</i>	DES- <i>r</i>	DES- <i>r</i>	DES- <i>i</i>	ATLAS- <i>o</i>	DES- <i>i</i>	DES- <i>g</i>	DES- <i>r</i>
5	ATLAS- <i>c</i>	DES- <i>r</i>	DES- <i>g</i>	DES- <i>i</i>	ATLAS- <i>o</i>	DES- <i>i</i>	DES- <i>g</i>	DES- <i>i</i>

in Eq. A1, we obtain a 5×5 -matrix:

$$[\Sigma_i]_{jk} = \underbrace{\sigma_{y_{1j}}^2 + \sigma_{y_{2j}}^2}_{\text{ATLAS } y_1 - \text{DES } y_2 \text{ error}} \delta(y_{2j}, y_{2k}) \\ + \underbrace{f'_k \sigma_{y_{2j}}^2 [\delta(y_{2j}, x_{1k}) - \delta(y_{2j}, x_{2k})] + f'_j \sigma_{y_{2k}}^2 [\delta(y_{2k}, x_{1j}) - \delta(y_{2k}, x_{2j})]}_{y_2 - \text{color}} \\ + \underbrace{f'_j f'_k \sigma_{x_{1j}}^2 [\delta(x_{1j}, x_{1k}) - \delta(x_{1j}, x_{2k})] - f'_j f'_k \sigma_{x_{2j}}^2 [\delta(x_{2j}, x_{1k}) - \delta(x_{2j}, x_{2k})]}_{\text{color} - \text{color}}. \quad (\text{A3})$$

Using this covariance matrix, we obtain an appropriate weights between each measurement within \mathbf{r}_i and collapse it into a single, representative offset value per star (generalized least-square estimation; GLS):

$$\bar{r}_i = \frac{\mathbf{1}^\top \Sigma_i^{-1} \mathbf{r}_i}{\mathbf{1}^\top \Sigma_i^{-1} \mathbf{1}}, \quad \sigma_{\bar{r},i}^2 = \frac{1}{\mathbf{1}^\top \Sigma_i^{-1} \mathbf{1}} \quad (\text{A4})$$

where $\sigma_{\bar{r},i}^2$ is the variance for \bar{r}_i , and $\mathbf{1} = (1, 1, \dots, 1)^\top$ is an all-one vector.

The obtained per-star offset value \bar{r}_i and its variance $\sigma_{\bar{r},i}^2$ is then used to evaluate our likelihood, which accounts for possible combinations of filters, their uncertainties, covariances, and overlapping use of data across such combinations:

$$\ln \mathcal{L}(\Delta_f, \sigma_{\text{int},f}) = \sum_i^{N_{\text{star}}} -\frac{1}{2} \left[\frac{(\bar{r}_i - \Delta_f)^2}{\sigma_{\bar{r},i}^2 + \sigma_{\text{int}}^2} + \ln(2\pi\sigma_{\bar{r},i}^2 + 2\pi\sigma_{\text{int}}^2) \right]. \quad (\text{A5})$$

This formula evaluates the likelihood of proposed offset for the ATLAS filter Δ_f (mag) against the par-star residual \bar{r}_i (mag) for each i -th star, which is derived from multiple combinations of filters between ATLAS and DES. We simultaneously measure the star-to-star intrinsic scatter σ_{int} .

B. PROFILE LIKELIHOOD FOR WAVELENGTH OFFSET

C. OPTIMAL SMOOTHING RADIUS DETERMINATION:

To determine our optimal smoothing radius we trained a model on 70% of the data from our calibration stars and then validated it with the remaining 30%. This process is done on each chip/ filter combo and the split is regenerated randomly four times for each combo. This results in Fig. 14, which shows the reduced chi squared as a function of smoothing radius. You can see that most of the chips are in the 250 - 750 pixel smoothing radius range for optimal reduced chi squared.

Our model functions as follows: it bins the data into 50x50 pixel chunks. It then convolves the binned data with a gaussian kernel (it ignores edge effects as these have a higher likelihood of being inaccurate by definition). Our model then uses the large scale structure of the CCD to correct for systematic offsets in the photometric residuals across the chip.

We used Fig. 14 to determine a median minimum chi squared across all chips, for which smoothing radius we should use for our correction model. We then apply the smoothing to the dataset which provides a correction to the dataset

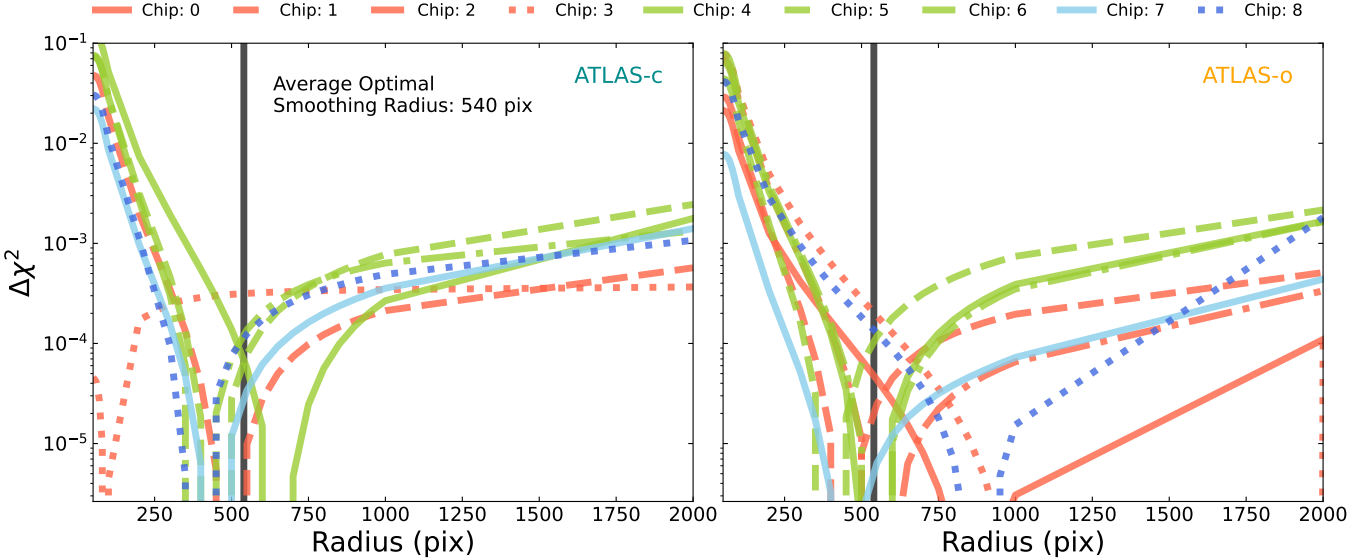


Figure 14. Cross validation plot of normalized chi squared vs smoothing radius in pixels. You can see the smoothing radius that minimizes the chi squared is focused around 540 pixels. We would rather slightly over bin (thus under correct) than under bin which would result in over correcting leading to potentially misleading and unrealistic trends. The y axis is reduced chi squared minus the minimum chi squared for each chip filter combo.

specifically correcting the chip 8 data without changing the rest of the chips data. This produces our intra-chip correction.

REFERENCES

- Abbott, D. C. T. M. C., Acevedo, M., Aguena, M., et al., 2024a, *The Astrophysical Journal Letters*, 973, 1, L14
 Abbott, D. C. T. M. C., Acevedo, M., Aguena, M., et al., 2024b, *The Astrophysical Journal Letters*, 973, 1, L14
 Acevedo, M., Sherman, N. F., Brout, D., et al., 2025, *The Dark Energy Bedrock All-Sky Supernova Program: Cross Calibration, Simulations, and Cosmology Forecasts*, arXiv:2508.10877
 Aleo, P. D., Malanchev, K., Sharief, S., et al., 2023, *ApJS*, 266, 1, 9, arXiv:2211.07128
 Bechtol, K., et al., 2025, *Dark Energy Survey Year 6 Results: Photometric Data Set for Cosmology*, no journal information available
 Bohlin, R. C., Gordon, K. D., Tremblay, P. E., 2014, *PASP*, 126, 942, 711, arXiv:1406.1707
 Boruah, S. S., Hudson, M. J., Lavaux, G., 2020, *MNRAS*, 498, 2, 2703, arXiv:1912.09383
 Boyd, B. M., Narayan, G., Mandel, K. S., et al., 2025, *MNRAS*, 540, 1, 385, arXiv:2412.08809
 Brout, D., Scolnic, D., Popovic, B., et al., 2022, *ApJ*, 938, 2, 110, arXiv:2202.04077
 Brout, D., Taylor, G., Scolnic, D., et al., 2022, *The Astrophysical Journal*, 938, 2, 111, ISSN 1538-4357
 Brout, D., Taylor, G., Scolnic, D., et al., 2022, *ApJ*, 938, 2, 111, arXiv:2112.03864
 Brown, B. A. A. H. S. K. P. P. T., Peter J., 2014, 354, 1, 89
 Burke, D. L., Rykoff, E. S., Allam, S., et al., 2017, *The Astronomical Journal*, 155, 1, 41
 Chen, P., Dong, S., Kochanek, C. S., et al., 2022, *ApJS*, 259, 2, 53, arXiv:2011.02461
 DESI Collaboration, Abdul Karim, M., Aguilar, J., et al., 2025, *PhRvD*, 112, 8, 083515, arXiv:2503.14738
 Filippenko, A. V., 2005, *Type Ia Supernovae and Cosmology*, 97–133, Springer Netherlands, Dordrecht
 Foley, R. J., Scolnic, D., Rest, A., et al., 2018, *MNRAS*, 475, 1, 193, arXiv:1711.02474
 Ganeshalingam, M., Li, W., Filippenko, A. V., et al., 2010, *The Astrophysical Journal Supplement Series*, 190, 2, 418
 Hamuy, M., Phillips, M. M., Suntzeff, N. B., et al., 1996, *AJ*, 112, 2438, arXiv:astro-ph/9609063
 Hicken, M., Challis, P., Jha, S., et al., 2009a, *ApJ*, 700, 1, 331, arXiv:0901.4787
 Hicken, M., Challis, P., Kirshner, R. P., et al., 2012, *ApJS*, 200, 2, 12, arXiv:1205.4493
 Hicken, M., Wood-Vasey, W. M., Blondin, S., et al., 2009b, *ApJ*, 700, 2, 1097, arXiv:0901.4804

- Jha, S., Kirshner, R. P., Challis, P., et al., 2006, AJ, 131, 1, 527, arXiv:astro-ph/0509234
- Koleva, M., Vazdekis, A., 2012, *Astronomy and Astrophysics*, 538, A143, ISSN 1432-0746
- Krisciunas, K., Contreras, C., Burns, C. R., et al., 2017, AJ, 154, 5, 211, arXiv:1709.05146
- Lyman, R., Cherubini, T., Businger, S., 2020, *Monthly Notices of the Royal Astronomical Society*, 496, 4, 4734, ISSN 0035-8711,
<https://academic.oup.com/mnras/article-pdf/496/4/4734/33503937/staa1787.pdf>
- Magnier, E. A., Schlafly, E. F., Finkbeiner, D. P., et al., 2020, ApJS, 251, 1, 6, arXiv:1612.05242
- Murakami, Y., Tweddle, J., Marlin, E., et al., 2025, TITAN: Type Ia Supernova Trove from ATLAS in the Nearby Universe. Overview and the data release of 10,000 light curves, in preparation
- Phillips, M. M., 1993, ApJL, 413, L105
- Popovic, B., Kenworthy, W. D., Ginolini, M., et al., 2025, arXiv e-prints, arXiv:2506.05471, arXiv:2506.05471
- Riess, A. G., Kirshner, R. P., Schmidt, B. P., et al., 1999, AJ, 117, 2, 707, arXiv:astro-ph/9810291
- Riess, A. G., Yuan, W., Macri, L. M., et al., 2022, ApJL, 934, 1, L7, arXiv:2112.04510
- Rigault, M., Smith, M., Goobar, A., et al., 2025, A&A, 694, A1, arXiv:2409.04346
- Rubin, D., Aldering, G., Betoule, M., et al., 2025, ApJ, 986, 2, 231, arXiv:2311.12098
- Rykoff, E. S., Tucker, D. L., Burke, D. L., et al., 2023
- Schlafly, E. F., Finkbeiner, D. P., Jurić, M., et al., 2012, The Astrophysical Journal, 756, 2, 158
- Scolnic, D., Brout, D., Carr, A., et al., 2022a, ApJ, 938, 2, 113, arXiv:2112.03863
- Scolnic, D., Brout, D., Carr, A., et al., 2022b, ApJ, 938, 2, 113, arXiv:2112.03863
- Scolnic, D., Casertano, S., Riess, A., et al., 2015, ApJ, 815, 2, 117, arXiv:1508.05361
- Sherman, N. F., Acevedo, M., Brout, D., et al., 2025, arXiv e-prints, arXiv:2508.10878, arXiv:2508.10878
- Stahl, B. E., Zheng, W., de Jaeger, T., et al., 2019, MNRAS, 490, 3, 3882, arXiv:1909.11140
- Tang, X. T., Brout, D., Karwal, T., Chang, C., Miranda, V., Vincenzi, M., 2025, Uniting the Observed Dynamical Dark Energy Preference with the Discrepancies in Ω_m and H_0 Across Cosmological Probes, arXiv:2412.04430
- Tonry, J. L., Denneau, L., Flewelling, H., et al., 2018, The Astrophysical Journal, 867, 2, 105
- Tonry, J. L., Denneau, L., Heinze, A. N., et al., 2018, PASP, 130, 988, 064505, arXiv:1802.00879
- Tripp, R., 1998, A&A, 331, 815
- Tweddle, J., Murakami, Y., Marlin, E., et al., 2025, TITAN: The Type Ia Supernova Trove from ATLAS in the Nearby Universe - Simulations and Bias Corrections, in preparation
- Vincenzi, M., Brout, D., Armstrong, P., et al., 2024, The Dark Energy Survey Supernova Program: Cosmological Analysis and Systematic Uncertainties, arXiv:2401.02945